WILEY-VCH

Exploring charged defects in ferroelectrics

by the switching spectroscopy piezoresponse force microscopy

Denis Alikin[*], Alexander Abramov, Anton Turygin, Anton Ievlev, Victoria Pryakhina,

Dmitry Karpinsky, Qingyuan Hu, Li Jin, Vladimir Shur, Alexander Tselev,

Andrei Kholkin[*]

D. Alikin, A. Abramov, A. Turygin, V. Pryakhina, V. Shur, A. Kholkin

School of Natural Sciences and Mathematics, Ural Federal University, Ekaterinburg, 620000, Russia

E-mail: denis.alikin@urfu.ru

A. Ievlev

Center for Nanophase Materials Sciences, Oak Ridge National Laboratory, Oak Ridge, 37830 USA

D. Karpinsky

Scientific-Practical Materials Research Centre of NAS of Belarus, Minsk, 220072, Belarus

Q. Hu, L. Jin

Electronic Materials Research Laboratory, Key Laboratory of the Ministry of Education & International Center for Dielectric Research, Xi'an Jiaotong University, Xi'an, 710049, China

A. Tselev, A. Kholkin

Department of Physics & CICECO, University of Aveiro, Aveiro 3810-193, Portugal

E-mail: kholkin@ua.pt

Keywords: defects, ferroelectrics, screening, bias field, domain walls, polarization reversal

Monitoring the charged defect concentration at the nanoscale is of critical importance for both the fundamental science and applications of ferroelectrics. However, up-to-date, high-resolution study methods of the investigation of structural defects, such as transmission electron microscopy, X-ray tomography, etc., are expensive and demand complicated sample preparation. With an example of the lanthanum-doped bismuth ferrite ceramics, we propose a novel method based on the switching spectroscopy piezoresponse force microscopy (SSPFM) that allows probing the electric potential from buried subsurface charged defects in the ferroelectric materials with a nanometer-scale spatial resolution. When compared with the composition-sensitive methods, such as neutron diffraction, X-ray photoelectron spectroscopy, and local time-of-flight secondary ion mass spectrometry, the SSPFM sensitivity to the variation of the electric potential from the charged defects is shown to be equivalent to less than 0.3 at. % of the defect concentration. Additionally, the possibility to locally evaluate dynamics of the polarization screening caused by the charged defects is demonstrated, which is of a significant interest for further understanding defect-mediated processes in ferroelectrics.

1. Introduction

Understanding surface defects becomes increasingly important in practical applications of oxides as electronic device sizes shrink closer to the atomic scale. In ferroelectric materials, precise control of the polarization reversal and hysteresis behavior at the nanoscale is a prerequisite for many applications, such as information storage,[1,2] memristors based on tunneling,[3,4] energy storage devices,[5] etc. Tailoring the defect structure permits fine-tuning of the functional properties of ferroelectrics.[6–10] The surfaces and interfaces are directly influenced by the nearby defects, and bulk properties are rendered by the defects via multiple mechanisms.[11,12] Up to date, the number of techniques allowing studies of defects with a high spatial resolution is limited, and they are mainly based on local monitoring of the crystalline structure or chemical composition.[13–15] Most of these local compositional methods like transmission electron microscopy, X-ray tomography, electron holography, etc. do not have a high enough sensitivity or need challenging sample preparation.[13] Thus, the novel experimental approaches allowing accurate measurement of the defect concentration and/or corresponded functional properties at the nanoscale are highly desirable.

In ferroelectrics, charged defects affect polarization reversal as they directly participate in the screening of the depolarization electric field[8,16–19] since they can become mobile under electric field.[17,20,21] In macroscopic measurements, charged defects manifest themselves as a shift of polarization versus electric field hysteresis loops, termed 'bias field' or 'imprint'.[22–25] and in

ferroelectric hysteresis loop doubling or "pinching".[16,26–29] Accumulation of charged defects at the domain walls and grain boundaries has been proven experimentally in bismuth ferrite by scanning transmission electron microscopy and conductive atomic force microscopy measurements.[11,12] Charged defects were shown to impact the interface conductivity and are believed to influence domain wall motion.[8,11,12]

In the beginning of the 90s, piezoresponse force microscopy (PFM) has been first used to study piezoelectric properties polarization reversal with a high spatial resolution down to a few nanometers.[30,31] The local switching can be performed by a conductive scanning probe miscopy tip with *in situ* monitoring of the piezoelectric response underneath the SPM probe tip biased by a varying voltage (so-called "switching spectroscopy" or "voltage spectroscopy").[32,33] In the switching spectroscopy, piezoresponse dependence on the applied DC voltage is represented as a local piezoelectric hysteresis loop.[32] The switching spectroscopy PFM (SSPFM) is often used for the spatially resolved studies of polarization heterogeneity in ferroelectrics and the analysis of materials response at individual interfaces.[32,34] By the analogy with the macroscopic piezoelectric hysteresis in ferroelectrics,[35] such parameters as bias voltage, coercive voltages, remnant piezoresponse, and piezoelectric offset can be extracted and analyzed.[32,36,37] The defect-mediated processes were also found to influence the shape of the hysteresis loop.[38,39]

In this work, working on La-doped $BiFeO_3$ (BLFO) polycrystalline ceramic samples, we demonstrate a complex approach to simultaneous measurements of the local piezoelectric response hysteresis loops together with the in-contact surface potential and reveal a relationship between the surface composition and piezoelectric response. The charged defects of different polarities (bismuth, iron, and oxygen vacancies identified from the spectroscopic analysis) get separated by the depolarization field of a ferroelectric and localized near the surface in domains with different orientations of the spontaneous polarization, which results in an electric potential varying across the ferroelectric surface. At the same time, the charged defects induce an internal bias electric field visible in the local hysteresis loops. Thus, the surface potential measured with an SPM tip in immediate contact with the ferroelectric surface can be used to determine the concentration of the charged defects at the ferroelectric surface at a level below 0.3 at.% of the defect concentration.

2. Results and discussion

2.1. Characterization of the material internal electric field

PFM measurements in a polycrystalline BLFO reveal ferroelectric domain structure, separated by either 180-degree or non-180-degree domain walls (Figure 1a,b). The 180-degree domain walls can be easily identified by their curved shape, while the non-180-degree domain walls are usually straight due to effects from elastic interactions.[40] First, we evaluated the spatial distribution of the polarization reversal behavior of the BLFO samples by the SSPFM (Figure 1e). For that, a region in the sample was mapped with a typical switching spectroscopy waveform (Figure 2a) of a 50 V maximal amplitude, a 5 ms-duration of each voltage pulse, and a 5 ms-off-field time gap. The initial PFM image of the ceramic sample before polarization reversal is shown in Figure 1b, while the same region after the SSPFM mapping is shown in Figure 1c.
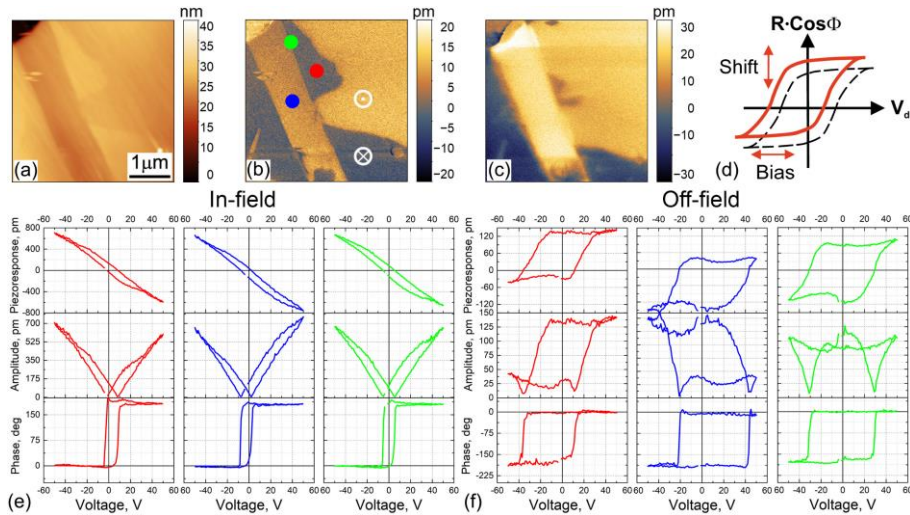

Figure 1. (a) Topography, and (b), (c) PFM images (b) before and (c) after the SSPFM. (d) Schematics illustrating the shift and bias of the local piezoeletric hysteresis loop.Examples of (e) on-field and (f) off-field local piezoelectric hysteresis loops obtained at the spots indicated by the circles of the corresponding colors in (b).

We start with the hysteresis loop acquisition from zero voltage bias with the application of increasing positive DC voltages and finish at zero bias with decreasing negative voltages on the probe (Figure 2a). In this case, it is expected that the polarization is aligned in the upward direction across the scanned area after the loop cycle. As seen in Figure 1c, it is generally not the case, however. The area with the upward-directed polarization significantly expanded after the loop cycle with the corresponding displacement of the domains wall. According to Figure 2c, the curved 180-degree domain wall moved, while the position of the straight non-180-degree domain wall was generally unchanged, which indicates that only 180-degree polarization reversal took place in a portion of the area of the scan. The lack of the non-180-degree switching

is probably caused by a significant clamping of the walls in the ceramic material, making difficult to reverse polarization locally because of the necessity to expand the crystal lattice of the grain as a result of the non-180-degree domain wall motion. In the bottom-left part of Figure 1c, the polarization state did not change, indicating either the absence of the polarization reversal or spontaneous polarization backswitching after removing the voltage from the probe. A typical hysteresis loop shape measured by the SSPFM is butterfly-like for amplitude and "nearly rectangular" saturated hysteresis in the piezoresponse ($R \cdot \cos\Phi$) signal (Figure 2b).[41] That naturally stems from the reversible nature of polarization with inversion of the sign of the piezoelectric displacement after polarization reversal. However, in our case, the shape of the off-field amplitude loops was nearly rectangular almost at every point. This shape can be understood if the phase signal is also taken into consideration [41,42]. Indeed, plotting the hysteresis loops of the piezoresponse signal shows that a transformation of the amplitude behavior from the butterfly-like shape to a nearly-rectangular-hysteresis is associated with a vertical shift of the piezoresponse loop (Figure 1d,1f). Importantly, the shift was dependent on the before-switching polarization orientation in the domains (Figure 1b). The shift was zero if the SSPFM was performed at the position of the domain wall (green loop in Figure 1f). A similar vertical shift of the hysteresis was observed earlier in thin-film and bulk materials, and the electrostatic force due to a surface potential was suggested to be responsible for the shift of the off-field hysteresis loops [43–46].
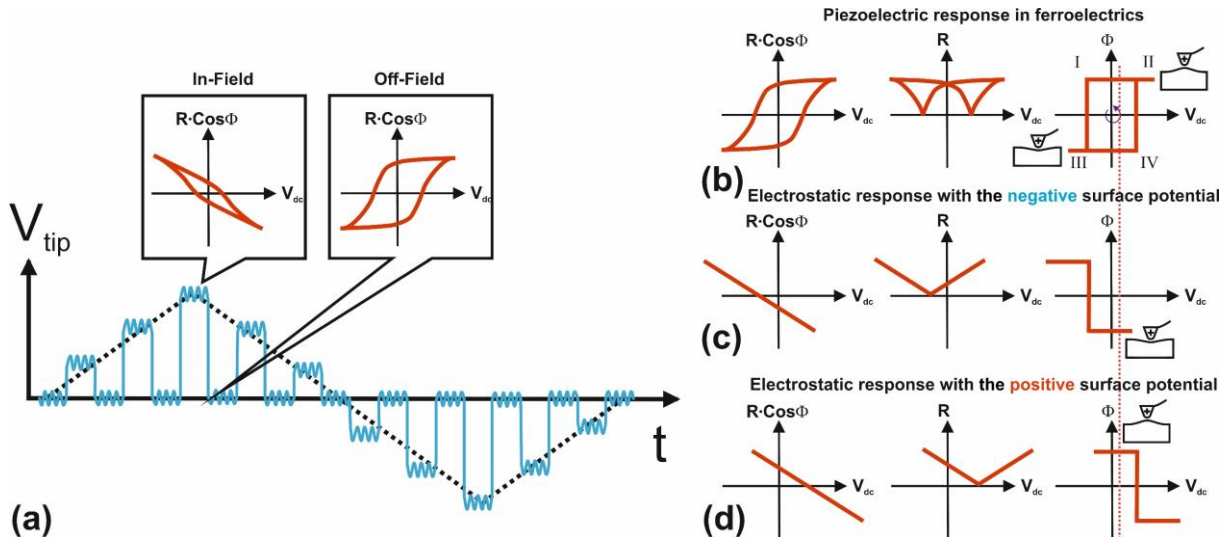

Figure 2. (a) Typical switching spectroscopy waveform and example of the piezoelectric hysteresis loops measured during electric field application (in-field) and after electric field drop-off (off-field). (b)-(d) Schematic dependence of the components of the electromechanical response (amplitude, R, phase, Φ, and the product $R \cdot \cos\Phi$) on the applied DC bias. The direction of the voltage sweep in hysteresis is the counterclockwise direction (indicated by the circled arrow). The dotted line indicates the position in the loop where the phase of the electromechanical response is captured in the positive half-period of the AC voltage applied to the tip.

It is known that electromechanical response in PFM of bulk ferroelectrics contains two major contributions: from the converse piezoelectric effect (D_{ac}^{piezo}) and electrostatic force appearing as a result of the local electrostatic interaction between the SPM tip and sample surface (D_{ac}^{elst}) [46–49]:

$$D_{ac}(V_{dc}) = D_{ac}^{piezo}(V_{dc}) + D_{ac}^{elst}(V_{dc}) = d_{eff}(V_{dc}) \cdot V_{ac} - k^{-1}C'V_{ac}\left(V_{dc} + V_{sp}(V_{dc})\right), \quad (1)$$

where V_{dc} and V_{ac} are DC and AC voltages, respectively, applied to the probe, d_{eff} is the effective piezoelectric coefficient, k is the tip-sample contact stiffness, C' is the coefficient depending on the capacitance gradient of the tip brought into contact with the sample surface. Here, the dependence of d_{eff} on V_{dc} comes from the polarization reversal followed by the formation of a domain with the reversed polarization and corresponding change of the value of the piezocoefficient from $-d_{eff}$ for the anti-parallel orientation to $+d_{eff}$ for the co-directed orientation of the polarization and the applied electric field. V_{sp} is the surface potential originating from a partially screened polarization bound charge and its screening charge [21]. Change of the surface potential can occur under a DC-voltage-biased tip due to disturbance of the surface screening layer, redistribution of the bulk charges, or introduction of the external charges from the SPM tip, i.e., charge injection [50].
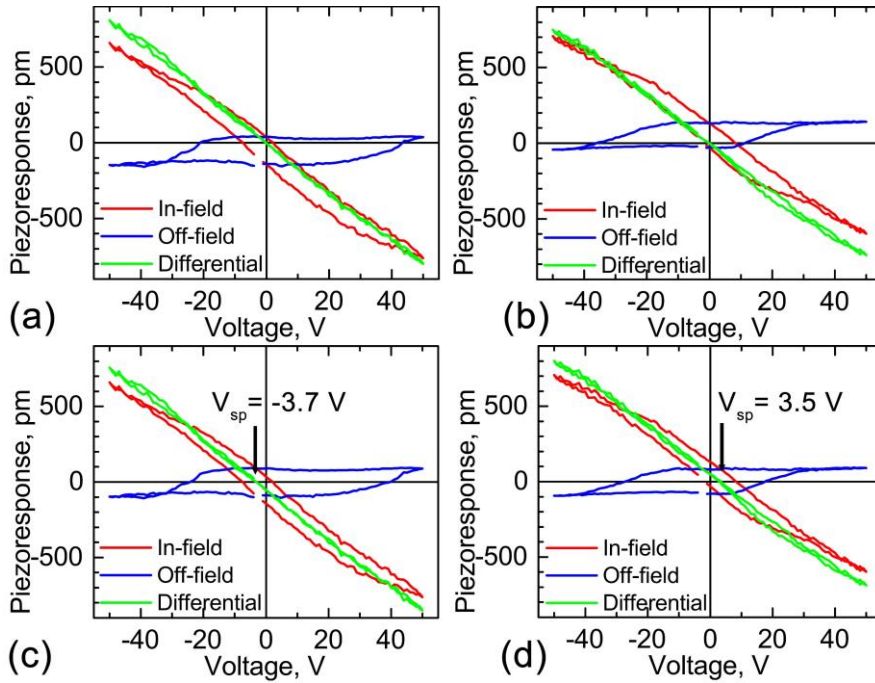

Figure 3. Examples of the acquired and derived hysteresis loops. In-field (red), off-field (blue), and differential loops (green) for hysteresis loops with different vertical shifts: (a) downshift, (b) upshift. In (c) and (d), the differential loops are calculated after the compensation of the hysteresis loop vertical shift. (a) and (c) correspond to the blue dot in Figure 1b, while (b) and (d) correspond to the red dot.

The overall electromechanical signal can be either sum or difference of the two terms in Eq. (1), depending on the sign of the surface potential and sign of the effective piezoelectric coefficient. These signs can be determined from the electromechanical response to the positive voltage applied to the probe [42,51]. The switching of the ferroelectric material by a positive voltage aligns its polarization along the electric field, and, as BLFO possesses a positive electrostriction coefficient, after that, the sample should expand under the action of a *positive* voltage at the SPM tip (Figure 2b). On the other hand, under the impact of a *negative* surface potential on the surface (Figure 2c), the positive voltage on the SPM tip results in the attraction of the tip to the surface, which is equivalent to the surface *contraction*. Thus, with the negative surface potential, the hysteresis loop should be shifted downwards along the response axis. Such shift is seen in the experimental result in Figure 1f (blue loop). In turn, in the neighboring domain in Figure 1b, where polarization is directed oppositely, the sign of the electrostatic force term in Eq. (1) is opposite due to a *positive* surface potential (Figure 2d), and the red loop in Figure 1f is shifted upwards. Recently, a similar conclusion regarding the contribution of the electrostatic force in the off-field PFM mode was made based on the measurements on thin BLFO films [46], however, the dependence on the polarization direction was not reported.

To extract information about the electrostatic force contribution, we calculated so-called "differential loops" by the subtraction of the off-field responses from the respective on-field response [52] (Figure 3a,b). The resulting differential loops are almost linear functions passing close to the reference system origin. As the acquired in- and off-field loops are shifted from the origin, this indicates that both in- and off-field loops should have identical shifts, which is nullified in the differential loops. With an account of this, the following procedure was implemented in order to extract the surface potential values from the loops: the rectangular-shaped off-field hysteresis loops were centered along the response axis to remove the vertical shifts, and, after that, the differential loops were recalculated (Figure 3c,d). The loop centering removes the contribution of the electrostatic force leaving only the contribution of the piezoresponse (the first term in Eq. 1). The recalculated differential loops reveal, thereby, the electrostatic force contribution due to the surface potential (the second term in Eq. 1), and the actual values of the surface potential can be extracted from the potential value that minimizes the electrostatic force (similar to the Kelvin probe force microscopy, KPFM [53]). In thus decoupled ferroelectric loops, a horizontal shift can be observed, which is related to the contribution of the internal electric field in the material rather than of the electrostatic force acting on the probe. The proposed scheme of the local in-contact electrostatic measurements

cancels out the electrostatic contribution from the bound polarization charge and shows solely the behavior of the charge responsible only for the built-in electric field.

This procedure of the response decomposition into the electrostatic force and piezoelectric parts was made for every pixel of the SSPFM map of the region in Figure 1. In Figure 4a,b, the resulting in-contact surface potential, V_{sp}, and C' coefficient are plotted. They were extracted by fitting the differential loops with the electrostatic force term of Eq. 1. In Figure 4c-h, different parameters of the centered off-field hysteresis loops are displayed: positive and negative coercive voltages V_{c+} and V_{c-}, the hysteresis bias voltage $V_b = \frac{1}{2}(V_{c+}+V_{c-})$, the effective piezoelectric coefficient d_{eff}, and the area of the hysteresis loop (which yields the energy dissipated for the full hysteresis cycle). The distributions of the surface potential in Figure 4a and hysteresis bias voltage in Figure 4e demonstrate anti-correlation following well a linear dependence as illustrated in Figure 4f.
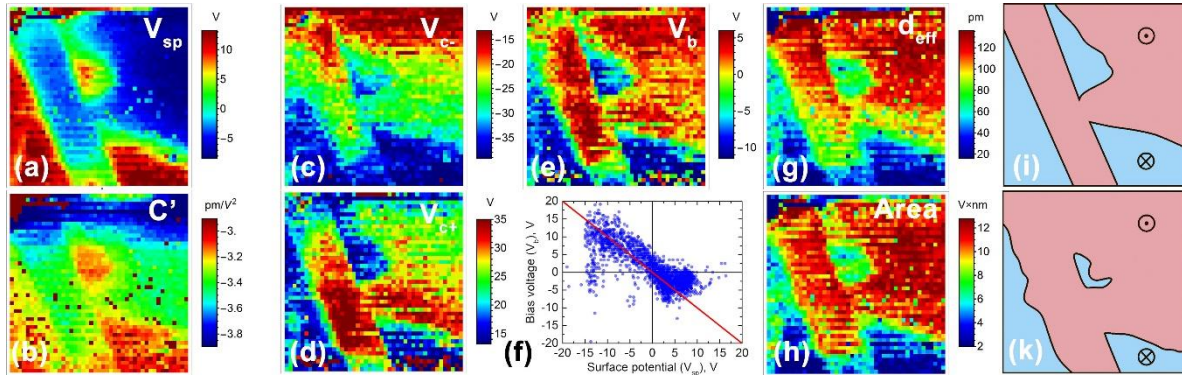

Figure 4. Mapping of the different parameters extracted from the hysteresis loops. (a) In-contact surface potential, (b) C' electrostatic force coefficient, (c) negative V_{c-} and (d) positive V_{c+} coercive voltages, (e) hysteresis loop bias voltage, V_b, (f) correlation between the bias voltage of the piezoelectric hysteresis loop, V_b, and surface potential, (g) effective piezoelectric coefficient, (h) piezoelectric losses (area of the hysteresis), (i) and (k) schemes illustrating the distribution of the polarization bound charge at the surface (i) before and (k) after SSPFM extracted from the PFM images in Figure 1b,c (red is positive charge, and blue is negative charge).

Local switching of the polarization within the dark regions in the PFM map in Figure 1b was triggered by a negative voltage, while the bright regions could be switched by a positive voltage. If the polarization is pointing up in the virgin state (like in the bright region), the bound polarization charge on the surface is positive, and it becomes negative after switching (Figure 4i,k, Figure 1b,c). At the same time, the hysteresis bias voltage remains unchanged after a few switching spectroscopy cycles. Thus, the observed hysteresis shift is not related to the bound charge creating the depolarization field within the domain. On the contrary, the shift is a result

of a material's internal electric field that is induced by some extrinsic charge, which screens the depolarization field in the original state of the sample[54,55].

As the built-in electric field can be directly associated with the surface adsorbates and/or defect state of the material, we further performed characterization of the material crystal structure and its surface chemical composition.

2.2. Structural and chemical characterization

X-ray diffraction and Neutron powder diffraction (NPD) were used to investigate the crystal structure and defect state in the bulk of the ceramics (see details in Supporting Information, Section 1). X-ray and neutron diffraction patterns confirmed the formation of a single-phase composition with a rhombohedral distortion of the unit cell. The calculated values of the ion occupation confirm the nearly stoichiometric composition of the material consistent with the chemical formula $Bi_{0.95}La_{0.05}FeO_3$. Thus, the amount of the defects in the material bulk is well below 1%, which is close to an accuracy of the NPD refinement. However, the defects are assumed to segregate at the surface, and the defect state of the material on the surface can significantly differ from bulk. Moreover, the stoichiometry of the BLFO can also be disrupted on the surface [56]. The local characterization of the surface defect state was done using complimentary ToF-SIMS, XPS, and EDS analysis. ToF-SIMS allows accurate depth profiling the element concentration, while the other two methods possess drastically different depth resolution. XPS probes up to a 5 nm-thick surface layer, while EDS captures signal from a depth up to 500-1000 nm from the surface.

ToF-SIMS sputtering profiles revealed a thin surface layer of adsorbates resolved as a large peak of the intensity near the surface (Supporting Information, Section 2). This layer showed a significant concentration of contaminants such as Na, K, and hydrocarbons, typical for samples exposed to ambient. This result was further confirmed by XPS measurement that indicated contamination of the surface by adventitious carbon: C-C, C-H, C-O groups (Figure 5c and Supporting Information, Figure S3). Signals of the contamination species decrease significantly with sputtering time, which proves that they are present only on the surface. ToF-SIMS depth profile shows that the thickness of the contamination layer is around 0.5-1 nm (Supporting Information, Figure S2a).
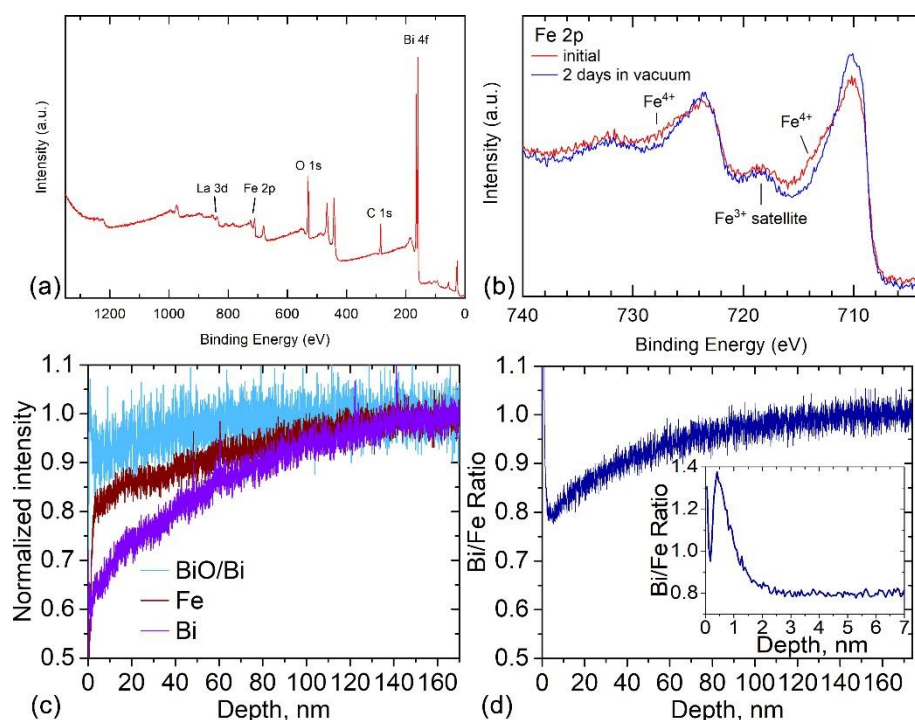
Figure 5. Chemical characterization of the BLFO surface layer. (a) XPS survey spectrum of BLFO. (b) Qualitative comparison of the Fe 2p core-level XPS spectra of the BLFO ceramics just after insertion in the vacuum camera of the spectrometer and after a 2 days vacuum exposure. (c), (d) ToF-SIMS sputtering profile of the (c) Bi, Fe ions, and BiO/Bi ions (oxygen concentration) and (d) Bi/Fe ratio (inset: zoomed 7 nm region at the surface).

To reveal the effect of the adsorbed layer on the surface potential, we performed conventional non-contact KPFM of the samples at a lift distance below 1 nm and obtained surface potential values at the level of hundreds of mV, which is much smaller than the values of a few volts extracted from the SSPFM differential loops (Figure 6). Such a large enhancement of surface potential measured in immediate contact of the tip with the surface implies that the layer of the surface adsorbate is disrupted by the probe in contact with the surface, which uncovers subsurface built-in charge in the material. At the same time, ToF-SIMS chemical maps do not reveal any spatial correlations between spontaneous polarization and distribution of adsorbates (Supporting Information, Figure S2b-d). Thus, adsorbates are assumed to act as neutral intermediate layer compensating the electric field from the sub-surface charge as schematically illustrated in Figure 7a.
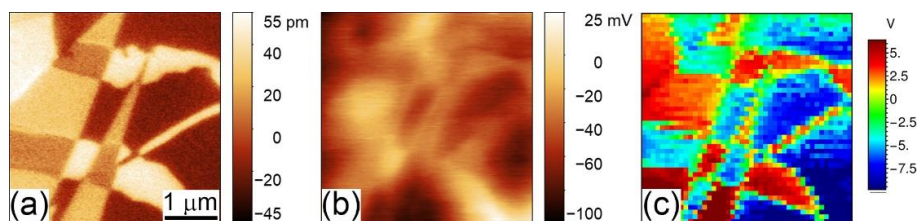

Figure 6. Comparison between (a) domain structure measured by PFM and surface potential measured (b) in the air (below 1 nm lift distance) by KPFM, (c) immediately in contact with the surface by SSPFM.

The sub-surface charge can be associated with the accumulation of charged defects near the surface [12,57] and/or alignment of the defect dipoles under the intrinsic domain depolarizing field [6,58,59]. The existence of the mobile charge defects in BFO is well-known, while details of the defect chemistry are still under discussion [8,60,61], because the defect composition is very sensitive to the atmosphere and sample preparation conditions [60,62,63]. The defect chemistry model assumes a formation of the different point defects in the bismuth ferrite, namely: oxygen, iron, and bismuth vacancies (see details in Supporting Information, Section 3).

XPS survey spectrum of BLFO demonstrates only signals from Bi, Fe, La, O, and surface carbon contamination (Figure 5a). A more detailed analysis of core-level bands can be found in Supporting Information, Section 3. The detailed analysis of the Fe 2p core level (Figure 5b) was performed to discriminate between Fe^{2+} and Fe^{4+} states at the surface (see Supporting Information, Section 3), associated with the reduction or oxidation reactions, respectively (see defect model in Supporting Information, Section 4). The features of the Fe 2p core-level spectra from the BLFO were perfectly overlayed with those from literature data [64]. However, both our spectrum and the one from ref. [64] were ~ 1.2 eV shifted to lower binding energies in respect to the Fe 2p peak positions in Fe_2O_3 and the position of the bands in the BFO single crystal [65], which was attributed to an influence of the net negative surface potential revealed in Figure 4a leading to the surface charge.
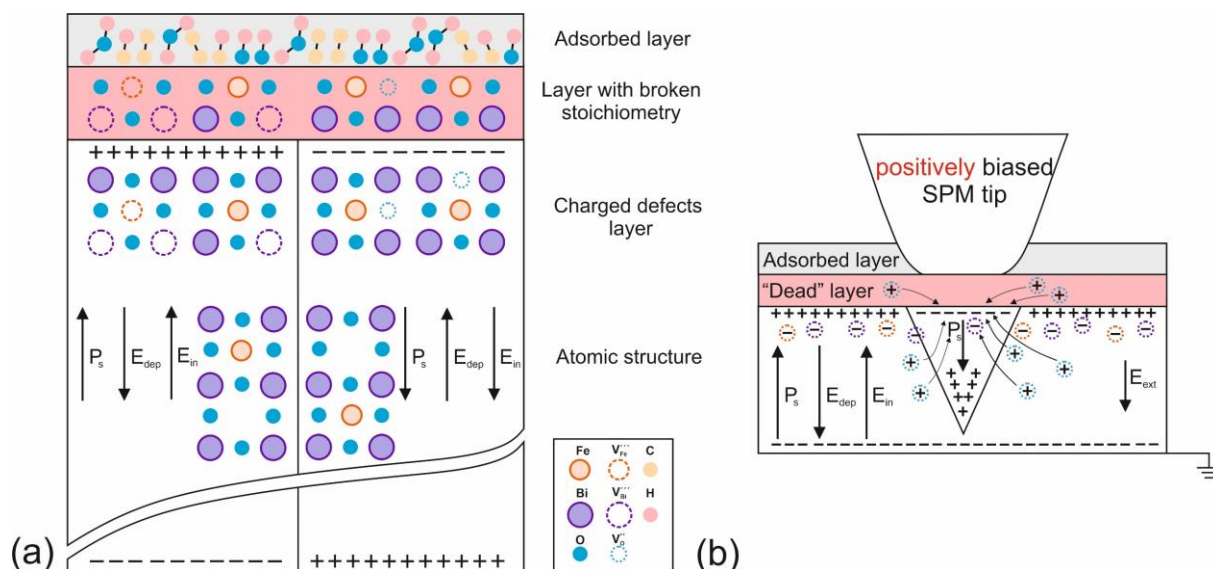

Figure 7. Schematics illustrating (a) the model of the BLFO surface structure. (b) A schematic illustrating electromigration of charged defects in the process of the new domain nucleation during the switching spectroscopy in the BLFO.

The comparison of the XPS spectra with the literature data of the different Fe-contain oxides allows to assume a formation of Fe^{4+} on the BLFO surface (see Supporting Information,

Section 3), which is likely occurs during the final steps of sample polishing with colloidal silica. According to the quantitative analysis, at least 5% of iron is in the Fe^{4+} oxidization state before exposure to vacuum, while a 2-days-long storage in vacuum leads to almost complete recovery of the surface iron into the Fe^{3+} state (Figure 5b). The Fe^{4+} state formed on the surface during the SSPFM measurements can be an indication of hole segregation (Supporting Information, Section 4, Equation S3), similar to that at domain walls and other interfaces in undoped BFO ceramics [11]. On the other hand, XPS did not reveal clear signs of Fe^{2+} associated with the reduction reaction (Supporting Information, Section 4, Equation S2).

Further insight into the chemistry of the surface layer was achieved using ToF-SIMS depth profiling, which allows studying the localization of the charged defects with an impressively high depth resolution below 1 nm. The depth profiles of the Fe, Bi, BiO/Bi , and Fe/B, are presented in Figure 5c,d. An around 1-2 nm-thick layer on the surface is related to the layer with disrupted stoichiometry. It contains a much higher amount of bismuth ions (Figure 5c,d), which is in line with the XPS elemental analysis (Table S2, Supporting Information, Section 3). In the subsurface layer, deeper 3-5 nm, the concentrations of bismuth and iron drop, which indicates the existence of the Bi and Fe vacancies on the surface. Deeper into the bulk, the concentration of ions smoothly grows, indicating recovery of the compositional stoichiometry. According to the EDS analysis probing much deeper in bulk, the concentration of the ions is close to the stoichiometric (Supporting Information, Section 3, Table S3), which is in accordance with the results of positron annihilation spectroscopy in BLFO revealed two characteristic lifetimes responsible for the iron and bismuth vacancies [66]. While the formation of the bismuth and iron vacancies should stimulate the appearance of the oxygen vacancies to keep the electroneutrality of the material, direct profiling of oxygen is challenging because of the use of oxygen ion beam for sputtering in these ToF-SIMS measurements. Therefore, the BiO/Bi ratio was used to trace oxygen ions inside the bulk (Figure 5c). A similar trend can be seen for BiO/Bi ratio with a drop in the 3-5 nm-thick subsurface layer and then a smooth recovery to the initial values towards the bulk. It can be concluded that an around 40-50 nm-thick defective layer with iron, bismuth, and oxygen vacancies lies underneath a 3-5 nm-thick layer with a disrupted stoichiometry.

2.3. Monitoring the dynamics of the charged defects and their contribution to the polarization screening

In this section, we apply the results of the previous analysis to interpret the local polarization switching behavior and to determine the concentration of the charged defects in the surface layer of our BLFO samples. ToF-SIMS sputtering profiles revealed an about 40-50 nm-thick

defective layer on the surface, which is close to the PFM probing depth. According to SSPFM results, the charged defects are spatially separated by the depolarization field of the domains. Thus, the positive and negative polarization bound charge near the surface should be screened by the charged defects of the opposite polarity. Based on the above chemical analysis of the surface, it can be proposed that the downward polarization can be screened by holes and positively charged oxygen vacancies ($V_O^{\cdot\cdot}$), while negatively charged iron (V_{Fe}''') and bismuth vacancies (V_{Bi}''') participate in the screening of the upward polarization (Figure 7a). Though the depolarization field can be partially reduced by the defect complexes with a dipole moment (defect dipoles) [6,58,59], their impact on the reduction of the depolarization field is seen to be minor because they have high activation energies for transport compared to the single charged defects [61].

The contribution of the charged defects to the dynamics of the polarization switching is dependent on defect mobility. According to the values of the activation energies for the different charged defects [15], the bismuth and iron vacancies should be immobile at room temperature, and they cannot move far from equilibrium positions under the action of the electric field from the probe. In turn, oxygen vacancies and holes are likely to be mobile in the external electric field. Thus, we measured hysteresis loops with longer DC voltage pulses and an increasing number of switching cycles. The reduction of the hysteresis loop horizontal and vertical shifts was observed when the duration of the voltage pulses in the SSPFM waveform (Figure 8a-d) and the number of switching spectroscopy cycles (Figure 8e,f) were increased. The variation of both parameters effectively increases the total time of the voltage pulse application. After five switching cycles, the amplitude hysteresis loops transformed from the square-shaped saturated-like to butterfly-shaped, indicating gradual removal of the internal electric field.
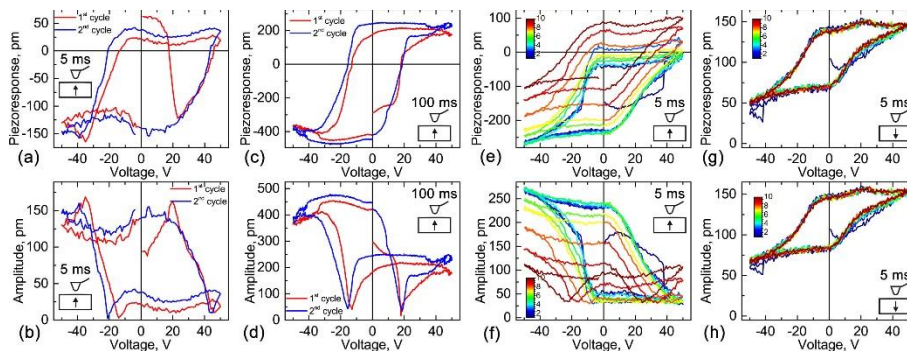

Figure 8. (a)-(d) Dependence of the hysteresis loop shape on the duration of the applied voltage pulses: (a), (b) 5ms; (c), (d) 100 ms. (e), (f) Transformation of the hysteresis loop shape during cycling. (a), (c), (e) Piezoresponse and (b), (d), (f) amplitude signals.

Importantly, the transformation of the hysteresis loop shape occurs only in the domains with upward oriented polarization in the virgin state (bright regions in Figure 1b), while in the

13

domains with downward oriented polarization (dark regions in Figure 1b), the shape of the hysteresis loop is conserved even after 10 cycles (Figure 8g,h). The gradual removal of the bias field in the hysteresis loop as a result of the increase of the total duration of the applied voltage pulse can be explained by the gradual screening of the material internal electric field by the migrating charge. This behavior is similar to that reported in the macroscopic measurements of the ferroelectric polarization loops, where the internal bias field gradually changes after polarization reversal.[24]

The application of the positive voltage to the tip reverses the polarization and creates a negative bound charge on the surface, which is added to the negative bias of the built-in screening charge (Figure 7b). As a "dead layer" with the absence of the ferroelectric polarization exists at the surface (Figure 7a), the "external" screening of the depolarization field by the electric charge induced on the SPM tip is likely incomplete. As such, the residual negative potential can attract positively charged oxygen vacancies and holes underneath the tip for the screening. In the case of the switching in the domains with downward directed polarization, the application of negative voltage induces a positive bound charge at the surface combined with the built-in positive screening charge from the localized oxygen vacancies. Thereby, migration of the negative charge underneath the tip should be induced to balance this positive charge. As mobilities of both bismuth and iron vacancies are very low [61], they cannot electro-migrate and compensate for the residual depolarization and built-in bias field. Obviously, partial screening of the residual depolarization field can be performed by the ejection of the oxygen vacancies localized in the region underneath AFM tip into the bulk. However, as the bias field does not show any significant change with the cycling in the downward oriented domains, we can assume that amount of the ejected oxygen vacancies is not enough to completely screen polarization in the area near the tip, and after voltage drop-off, spontaneous backswitching happens, and oxygen vacancies return to the initial place. The backswitching can be seen in the difference of the piezoelectric losses (measured as the area of the hysteresis) and effective piezoelectric coefficient in the domains with differently oriented polarization (Figure 4g,h). The domain with upward polarization direction reveals significantly lower values of the piezoelectric losses and effective piezoelectric coefficient, which shows almost complete backswitching of the polarization. At the same time, near-zero in-contact surface potential was observed after SSPFM in the area crossed by the wall during its displacement (compare maps in Figure 1b,c and Figure 3a,b). Thus, the motion of the domain wall is accompanied with neutralization of the extrinsic charge, while in the scanned regions with downward polarization, where the extrinsic charge was not fully removed, spontaneous polarization backswitching

occurs after the switching spectroscopy. Similar results of the spontaneous backswitching of the domains with the downward direction of the polarization were also observed in the experiments with the local switching by the single rectangular voltage pulses (see Supporting Information, Section 5). Thus, the behavior of the internal electric field during the local polarization reversal confirms the difference between the charged defect screening in the domains with opposite direction of the polarization.

If the defect chemistry of the surface is known, SSPFM can be used for the quantitative measurements of the charged defect concentration. To estimate the sensitivity of the SSPFM to the variation of surface defect concentration, finite element simulations were performed (Figure 9). The domain was modeled as a charged disc in the subsurface layer of the ferroelectric sample with the lateral size equal to the tip radius, 40 nm depth corresponding to the depth of the defective layer, and a constant charge density (Figure 9a). The charge density was adjusted to match the surface potentials obtained in the model and in the experiment. The surface potential corresponds to the tip bias voltage at which the electrostatic force acting on the tip from the charged disc and the bottom counter electrode is minimal. With the surface potential of about 10 V as measured experimentally by the SSPFM, we obtained the charge density of around 2.2 μC/cm^2, which is equivalent to about 0.2 % of oxygen vacancies per unit cell (assuming solely oxygen vacancies taking part in the polarization screening). This implies that the sensitivity of the SSPFM is much higher than that of many other methods for characterization of surface chemical composition, and its lateral resolution is limited only by the tip diameter.
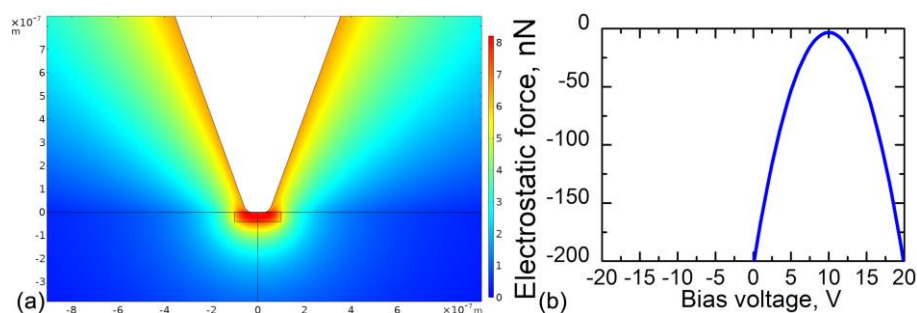

Figure 9. Result of the finite element simulations in COMSOL Multiphysics software of the electrostatic tip-surface interaction in the presence of the charged surface layer (charge disc). (a) Electric potential distribution with 6.8 V bias voltage at SPM probe. (b) The electrostatic force acting on the tip depends on the bias voltage applied to the probe.

3. Conclusion

In summary, a novel method based on the switching spectroscopy PFM was introduced, which allows identification of the charged defect distribution along the material surface with a high spatial resolution. The discussed method is based on the decoupling of the electrostatic and true piezoelectric responses in the local electromechanical response measured by the probe tip in contact with the surface. The surface potential extracted from the local electrostatic signal measured in contact with the surface was shown to be due to charged defects localized in the subsurface material layer, which is confirmed by the chemical methods: XPS and ToF-SIMS. The charged defects directly take part in the screening of the ferroelectric polarization. The localized screening charge is responsible for the built-in internal electric field, which can be probed separately as a bias of the local piezoelectric hysteresis loop. The sensitivity of the electrostatic force measurements to the charge defect concentration was estimated by the finite element simulations and is below 0.3 at.%.

Besides, SSPFM allows *in situ* time-resolved observation of the charged defect redistribution. The polarization bound charge in the domains with the different orientation of the spontaneous polarization was shown to accumulate charged defects of different polarities: negative bismuth ion vacancies screen positive polarization charge, while positive oxygen vacancies and holes screen negative polarization charge. The field-induced behavior of these charged defects during local polarization switching becomes crucial in the dynamics of the polarization screening. The mobile oxygen vacancies and holes were shown to stabilize forming domain patterns by screening the residual depolarization field. In contrast, immobile defects induce the internal bias field impeding polarization reversal and stimulating spontaneous backswitching. As such, the introduced method allows not only probing charged defect distribution but also inspecting polarization screening dynamics, which is believed to give an essential insight into the mechanisms of interface-related phenomena in ferroelectric materials.

4. Experimental Section/Methods

Sample synthesis and preparation: Bulk samples of the polycrystalline $BiFeO_3$ doped with 5% La were sintered using a two-stage solid-phase synthesis. The details of the sample preparation can be found in ref. [67] Before SPM measurements, the sample surface was polished step-by-step, decreasing the particle size of a diamond paste abrasive down to 0.25 μm. Fine polishing with an alkali-based solution of 60 nm-size colloidal silica (SF1 Polishing

Suspension, Logitech, United Kingdom) was performed for one hour to remove the mechanically strained region from the sample surface that can appear after previous polishing steps.

Bulk structure characterization: The X-ray and neutron diffraction data from the samples were collected at room temperature using, respectively, a Rigaku D/MAX-B diffractometer with the Cu-Kα radiation and the neutron powder diffractometer E9 Firepod, λ=1.7977Å, at Helmholtz-Zentrum Berlin. Diffraction data were analyzed by the Rietveld method using the FullProf software package.[68]

Piezoresponse force microscopy (PFM) and spectroscopy: The out-of-plane PFM measurements and spectroscopy were carried out with an MFP-3D SA scanning probe microscope (Oxford Instruments, UK) in the Dual AC Resonance Tracking (DART) mode at the frequency of the first flexural contact resonance of the cantilever probe around 1.4 MHz. The measurements were done with an internal lock-in amplifier. An AC voltage of 5 V applied to the SPM probe was combined with the switching spectroscopy waveform. The waveform is a sequence of rectangular voltage pulses with a triangular-wave-shaped amplitude envelope, with the voltage set to zero after each voltage pulse.[69] The width of voltage pulses in the switching spectroscopy waveform was constant and varied from 5 ms to 100 ms from run to run. Processing of the spectroscopy data was carried out using a homemade code written in Wolfram Mathematica. The array of the data points acquired during one voltage spectroscopy pulse was split into on- and off-field hysteresis loops. The on-field hysteresis loops were constructed from the data points acquired during the voltage pulses, and the off-field hysteresis loops were constructed from the data points acquired in-between the voltage pulses. Around 1 ms of data points right after the beginning and end of each switching pulse was ignored in the analysis for all hysteresis loops to remove effects of transient processes influencing the final hysteresis loop shape. The phase offset of the lock-in amplifier was adjusted equally across the whole array of the hysteresis loops. The lock-in

amplitude (R) and phase (Φ) signals were represented as $R \cdot cos\Phi$ and $R \cdot sin\Phi$, which we call here "piezoresponse signals". After that, the $R \cdot sin\Phi$ signal was minimized to accumulate the full response in the $R \cdot cos\Phi$ signal by adjusted the phase Φ following the procedure from refs. [70,71]. HA_NC (ScanSens, Germany) probes with a 35 nm radius of curvature, 12 N/m spring constant, and conductive W_2C coating were used for all measurements. A controllable atmosphere with a relative humidity below 5 % was maintained in the microscope chamber using constant flow of dry nitrogen.

Kelvin probe force microscopy (KPFM): Conventional KPFM was done using internal amplitude-modulated double-pass KPFM mode of MFP-3D SA scanning probe microscope (Oxford Instruments, UK) with the same probes. The measurements were performed at the frequency of the first flexural free resonance. The lift distance was set to zero, which implies the real distance between the tip and surface was below 1 nm. The surface touch was excluded by scanning the flat region and adjusting the electric field-induced tip oscillation to be lower than tapping-mode amplitude at the first pass. HA_NC (ScanSens, Germany) probes with a 35 nm radius of curvature, 12 N/m spring constant, and conductive W_2C coating were used for all measurements. A controllable atmosphere with a relative humidity below 5 % was maintained in the microscope chamber using constant flow of dry nitrogen.

Time-of-flight secondary ion mass spectrometry (ToF-SIMS): Chemical characterization of the sample surface was carried out using ToF-SIMS. The measurements were performed in the positive ion detection mode with a TOF SIMS-5 instrument (ION-TOF GmbH, Germany). A Bi^{3+} ion beam with an energy of 30 keV, a current of ~0.5 nA, and a spot size of ~100 nm was used as a primary source. An O_2- ion gun of 1keV energy and a current of ~250 nA was used as a sputter source for depth profiling. AFM calibration with an integrated AFM after sputtering revealed a sputter rate of about 0.0036 pm/s. Chemical imaging was carried out in the non-interlaced mode, where every SIMS scan by primary gun ions was followed by a

sputtering cycle. A low-energy electron flood gun with a current ~10 uA was used in a pulsed mode for charge compensation between the scanning cycles.

X-ray photoelectron spectroscopy (XPS): XPS measurements were carried out using a Thermo Scientific K-Alpha+ system with a monochromatic Al Kα source (hν = 1460 eV) and the beam focused in a 400 μm diameter spot. The instrument was calibrated to the Au $4f_{7/2}$ core level binding energy of 83.9 eV. The carbon contamination peak was at 284.6 eV. The charge neutralizer system was used for analysis. The chamber pressure was about $5 \cdot 10^{-7}$ mbar. Collected XPS spectra were analyzed using the Avantage ThermoScientific software (ver. 5.992). The XPS peaks were approximated using Lorentzian/Gaussian (30%) functions after the Shirley-type background subtraction.

Energy Dispersive Spectroscopy (EDS): EDS was performed at AURIGA CrossBeam workstation (Carl Zeiss, Germany) scanning electron microscope equipped with INCA analysis system (Oxford Instruments, UK).

Finite element (FE) simulations: FE simulations were made using the electrostatics module of COMSOL Multiphysics software. The electrostatic force acting on the probe tip was calculated via integration of the vertical component of the Maxwell stress over the probe surface.

Supporting Information

Supporting Information is available from the Wiley Online Library or from the author.

Received: ((will be filled in by the editorial staff))

Revised: ((will be filled in by the editorial staff))

Published online: ((will be filled in by the editorial staff))

References

[1] A. Q. Jiang, Y. Zhang, *NPG Asia Mater.* **2019**, *11*, 2.

[2] A. Q. Jiang, W. P. Geng, P. Lv, J. Hong, J. Jiang, C. Wang, X. J. Chai, J. W. Lian, Y. Zhang, R. Huang, D. W. Zhang, J. F. Scott, C. S. Hwang, *Nat. Mater.* **2020**, *19*, 1188.

[3] H. Lu, A. Lipatov, S. Ryu, D. J. Kim, H. Lee, M. Y. Zhuravlev, C. B. Eom, E. Y. Tsymbal, A. Sinitskii, A. Gruverman, *Nat. Commun.* **2014**, *5*, 5518.

[4] P. Maksymovych, S. Jesse, P. Yu, R. Ramesh, A. P. Baddorf, S. V Kalinin, *Science* **2009**, *324*, 1421.

[5] Q. Hu, Y. Tian, Q. Zhu, J. Bian, L. Jin, H. Du, D. O. Alikin, V. Y. Shur, Y. Feng, Z. Xu, X. Wei, *Nano Energy* **2020**, *67*, 104264.

[6] D. Lee, B. C. Jeon, S. H. Baek, S. M. Yang, Y. J. Shin, T. H. Kim, Y. S. Kim, J.-G. Yoon, C. B. Eom, T. W. Noh, *Adv. Mater.* **2012**, *24*, 6490.

[7] Z. Li, H. Thong, Y. Zhang, Z. Xu, Z. Zhou, Y. Liu, Y. Cheng, S. Wang, C. Zhao, F. Chen, K. Bi, B. Han, K. Wang, *Adv. Funct. Mater.* **2021**, *31*, 2005012.

[8] A. Bencan, G. Drazic, H. Ursic, M. Makarovic, M. Komelj, T. Rojac, *Nat. Commun.* **2020**, *11*, 1762.

[9] P. Barrozo, D. R. Småbråten, Y. Tang, B. Prasad, S. Saremi, R. Ozgur, V. Thakare, R. A. Steinhardt, M. E. Holtz, V. A. Stoica, L. W. Martin, D. G. Schlom, S. M. Selbach, R. Ramesh, *Adv. Mater.* **2020**, *32*, 2000508.

[10] M. Makarovic, N. Kanas, A. Zorko, K. Ziberna, H. Ursic, D. R. Smabraten, S. M. Selbach, T. Rojac, *J. Eur. Ceram. Soc.* **2020**, *40*, 5483.

[11] T. Rojac, A. Bencan, G. Drazic, N. Sakamoto, H. Ursic, B. Jancar, G. Tavcar, M. Makarovic, J. Walker, B. Malic, D. Damjanovic, *Nat. Mater.* **2017**, *16*, 322.

[12] D. Alikin, Y. Fomichov, S. P. Reis, A. Abramov, D. Chezganov, V. Shur, E. Eliseev, S. V. Kalinin, A. Morozovska, E. B. Araujo, A. Kholkin, *Appl. Mater. Today* **2020**, *20*,

100740.

[13]   F. Gunkel, D. V. Christensen, Y. Z. Chen, N. Pryds, *Appl. Phys. Lett.* **2020**, *116*, 120505.

[14]   M. Setvín, M. Wagner, M. Schmid, G. S. Parkinson, U. Diebold, *Chem. Soc. Rev.* **2017**, *46*, 1772.

[15]   F. A. Selim, *Mater. Charact.* **2021**, *174*, 110952.

[16]   Z.-H. Zhao, Y. Dai, F. Huang, *Sustain. Mater. Technol.* **2019**, *20*, e00092.

[17]   I. S. Vorotiahin, A. N. Morozovska, Y. A. Genenko, *Acta Mater.* **2020**, *184*, 267.

[18]   W. R. Geng, X. H. Tian, Y. X. Jiang, Y. L. Zhu, Y. L. Tang, Y. J. Wang, M. J. Zou, Y. P. Feng, B. Wu, W. T. Hu, X. L. Ma, *Acta Mater.* **2020**, *186*, 68.

[19]   C. Becher, L. Maurel, U. Aschauer, M. Lilienblum, C. Magén, D. Meier, E. Langenberg, M. Trassin, J. Blasco, I. P. Krug, P. a. Algarabel, N. a. Spaldin, J. a. Pardo, M. Fiebig, *Nat. Nanotechnol.* **2015**, *10*, 661.

[20]   S. V. Kalinin, Y. Kim, D. D. Fong, A. N. Morozovska, *Reports Prog. Phys.* **2018**, *81*, 036502.

[21]   S. Hong, S. M. Nakhmanson, D. D. Fong, *Reports Prog. Phys.* **2016**, *79*, 076501.

[22]   G. Arlt, H. Neumann, *Ferroelectrics* **1988**, *87*, 109.

[23]   S. Kim, V. Gopalan, K. Kitamura, Y. Furukawa, *J. Appl. Phys.* **2001**, *90*, 2949.

[24]   V. Ya. Shur, A. R. Akhmatkhanov, I. S. Baturin, M. S. Nebogatikov, M. A. Dolbilov, *Phys. Solid State* **2010**, *52*, 2147.

[25]   Y. Zhang, I. S. Baturin, E. Aulbach, D. C. Lupascu, A. L. Kholkin, V. Y. Shur, J. Rödel, *Appl. Phys. Lett.* **2005**, *86*, DOI 10.1063/1.1847712.

[26]   E. G. Lee, D. J. Wouters, G. Willems, H. E. Maes, *Appl. Phys. Lett.* **1996**, *69*, 1223.

[27]   T. Schenk, E. Yurchuk, S. Mueller, U. Schroeder, S. Starschich, U. Böttger, T. Mikolajick, *Appl. Phys. Rev.* **2014**, *1*, 041103.

[28]   X. Ren, *Nat. Mater.* **2004**, *3*, 91.

[29]   E. T. Wefring, M. A. Einarsrud, T. Grande, *Phys. Chem. Chem. Phys.* **2015**, *17*, 9420.

[30]   H. Birk, *J. Vac. Sci. Technol. B Microelectron. Nanom. Struct.* **1991**, *9*, 1162.

[31]   P. Güthner, K. Dransfeld, P. Gljthner, K. Dransfeld, U. Konstanz, F. Physik, D.-Konstanz, **1992**, *1137*, DOI 10.1063/1.107693.

[32]   S. Jesse, A. P. Baddorf, S. V. Kalinin, *Appl. Phys. Lett.* **2006**, *88*, 21.

[33]   R. K. Vasudevan, S. Jesse, Y. Kim, A. Kumar, S. V. Kalinin, *MRS Commun.* **2012**, *2*, 61.

[34]   P. Bintachitt, S. Trolier-McKinstry, K. Seal, S. Jesse, S. V. Kalinin, *Appl. Phys. Lett.*

2009, *94*, 042906.

[35] A. L. Kholkin, C. Wütchrich, D. V. Taylor, N. Setter, *Rev. Sci. Instrum.* **1996**, *67*, 1935.

[36] S. Jesse, H. N. Lee, S. V. Kalinin, *Rev. Sci. Instrum.* **2006**, *77*, DOI 10.1063/1.2214699.

[37] S. V. Kalinin, B. J. Rodriguez, S. Jesse, Y. H. Chu, T. Zhao, R. Ramesh, S. Choudhury, L. Q. Chen, E. A. Eliseev, A. N. Morozovska, *Proc. Natl. Acad. Sci.* **2007**, *104*, 20204.

[38] A. N. Morozovska, S. V. Svechnikov, E. A. Eliseev, B. J. Rodriguez, S. Jesse, S. V. Kalinin, *Phys. Rev. B* **2008**, *78*, 054101.

[39] S. V. Kalinin, S. Jesse, B. J. Rodriguez, Y. H. Chu, R. Ramesh, E. A. Eliseev, A. N. Morozovska, *Phys. Rev. Lett.* **2008**, *100*, 155703.

[40] D. Alikin, A. Turygin, A. Kholkin, V. Shur, *Materials (Basel).* **2017**, *10*, 47.

[41] N. Balke, P. Maksymovych, S. Jesse, A. Herklotz, A. Tselev, C. B. Eom, I. I. Kravchenko, P. Yu, S. V. Kalinin, *ACS Nano* **2015**, *9*, 6484.

[42] A. D. U. and V. Y. S. Denis O. Alikin, Boris N. Slautin, *IEEE Trans. Dielectr. Electr. Insul.* **n.d.**

[43] K. Seal, S. Jesse, M. P. Nikiforov, S. V. Kalinin, I. Fujii, P. Bintachitt, S. Trolier-McKinstry, *Phys. Rev. Lett.* **2009**, *103*, 057601.

[44] Q. Li, Y. Liu, J. Schiemer, P. Smith, Z. Li, R. L. Withers, Z. Xu, *Appl. Phys. Lett.* **2011**, *98*, 092908.

[45] S. Guo, O. S. Ovchinnikov, M. E. Curtis, M. B. Johnson, S. Jesse, S. V. Kalinin, *J. Appl. Phys.* **2010**, *108*, 084103.

[46] H. Qiao, O. Kwon, Y. Kim, *Appl. Phys. Lett.* **2020**, *116*, 172901.

[47] A. Gomez, T. Puig, X. Obradors, *Appl. Surf. Sci.* **2018**, *439*, 577.

[48] E. Soergel, *J. Phys. D. Appl. Phys.* **2011**, *44*, 464003.

[49] S. Kim, D. Seol, X. Lu, M. Alexe, Y. Kim, *Sci. Rep.* **2017**, *7*, 41657.

[50] N. Balke, P. Maksymovych, S. Jesse, I. I. Kravchenko, Q. Li, S. V Kalinin, *ACS Nano* **2014**, *8*, 10229.

[51] Q. N. Chen, S. B. Adler, J. Li, *Appl. Phys. Lett.* **2014**, *105*, 1.

[52] N. Balke, S. Jesse, B. Carmichael, M. B. Okatan, I. I. Kravchenko, S. V Kalinin, A. Tselev, *Nanotechnology* **2017**, *28*, 065704.

[53] W. Melitz, J. Shen, A. C. Kummel, S. Lee, *Surf. Sci. Rep.* **2011**, *66*, 1.

[54] V. Ya. Shur, E. L. Rumyantsev, *Ferroelectrics* **1997**, *191*, 319.

[55] X. Liu, K. Kitamura, K. Terabe, H. Zeng, Q. Yin, *Appl. Phys. Lett.* **2007**, *91*, 232913.

[56] J. Dong, X. Zhang, Y. Wang, Y. Gong, P. An, H. Li, Z. Guo, X. Hao, Q. Jia, D. Chen, *J. Phys. Condens. Matter* **2019**, *31*, 085402.

[57] I. Stolichnov, M. Iwanowska, E. Colla, B. Ziegler, I. Gaponenko, P. Paruch, M. Huijben, G. Rijnders, N. Setter, *Appl. Phys. Lett.* **2014**, *104*, 132902.

[58] I. Bretos, R. Jiménez, C. Gutiérrez-Lázaro, I. Montero, M. L. Calzada, *Appl. Phys. Lett.* **2014**, *104*, 092905.

[59] B. Zhao, Z. Chen, J. Meng, H. Lu, D. W. Zhang, A. Jiang, *J. Appl. Phys.* **2015**, *117*, 204103.

[60] M. Schrade, N. Masó, A. Perejón, L. A. Pérez-Maqueda, A. R. West, *J. Mater. Chem. C* **2017**, *5*, 10077.

[61] G. Geneste, C. Paillard, B. Dkhil, *Phys. Rev. B* **2019**, *99*, 024104.

[62] T. Rojac, A. Bencan, B. Malic, G. Tutuncu, J. L. Jones, J. E. Daniels, D. Damjanovic, *J. Am. Ceram. Soc.* **2014**, *97*, 1993.

[63] M. I. Morozov, M. A. Einarsrud, T. Grande, *J. Appl. Phys.* **2014**, *115*, 0.

[64] N. S. Bein, P. Machado, M. Coll, F. Chen, M. Makarovic, T. Rojac, A. Klein, *J. Phys. Chem. Lett.* **2019**, *10*, 7071.

[65] A. T. Kozakov, A. G. Kochur, K. A. Googlev, A. V. Nikolsky, I. P. Raevski, V. G. Smotrakov, V. V. Yeremkin, *J. Electron Spectros. Relat. Phenomena* **2011**, *184*, 16.

[66] W. Ge, A. Rahman, H. Cheng, M. Zhang, J. Liu, Z. Zhang, B. Ye, *J. Magn. Magn. Mater.* **2018**, *449*, 401.

[67] D. V. Karpinsky, I. O. Troyanchuk, M. Tovar, V. Sikolenko, V. Efimov, A. L. Kholkin, *J. Alloys Compd.* **2013**, *555*, 101.

[68] J. Rodríguez-Carvajal, *Phys. B Condens. Matter* **1993**, *192*, 55.

[69] S. Hong, J. Woo, H. Shin, J. U. Jeon, Y. E. Pak, E. L. Colla, N. Setter, E. Kim, K. No, *J. Appl. Phys.* **2001**, *89*, 1377.

[70] N. Balke, S. Jesse, Q. Li, P. Maksymovych, M. Baris Okatan, E. Strelcov, A. Tselev, S. V. Kalinin, *J. Appl. Phys.* **2015**, *118*, 072013.

[71] T. Jungk, Á. Hoffman, E. Soergel, *J. Microsc.* **2007**, *227*, 72.

The novel method to probe the charged defect using decoupling of the electrostatic and pure piezoelectric contribution in the switching spectroscopy piezoresponse force microscopy is introduced. Combining easy realization, high spatial resolution, and large sensitivity it provides powerful tool for researchers to study the defect-mediated phenomena in ferroelectric at the nanoscale.

D. Alikin*, A. Abramov, A. Turygin, A. Ievlev, V. Pryakhina, .D. Karpinsky, Q. Hu, L. Jin, V. Shur, A. Tselev, A. Kholkin*

Exploring charged defects in ferroelectrics
by the switching spectroscopy piezoresponse force microscopy
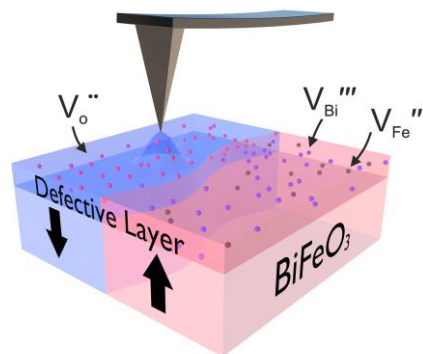
Supporting Information

Exploring charged defects in ferroelectrics

by the switching spectroscopy piezoresponse force microscopy

Denis Alikin[*]*, Alexander Abramov, Anton Turygin, Anton Ievlev, Victoria Pryakhina, Dmitry Karpinsky, Qingyuan Hu, Li Jin, Vladimir Shur, Alexander Tselev, Andrei Kholkin*[*]

1. X-ray diffraction and Neutron powder diffraction (NPD) characterization

X-ray diffraction and Neutron powder diffraction (NPD) were used to investigate the crystal structure and defect state of the bulk ceramic material. The X-ray and neutron diffraction patterns confirmed the formation of a single-phase composition with a rhombohedral distortion of the unit cell. The diffraction patterns were successfully refined, assuming a rhombohedral structure with the space group *R3c*, the same as in undoped $BiFeO_3$ (BFO) [1]. The neutron diffraction spectrum of the sample refined using Rietveld method is presented in Figure S1. The unit cell parameters show an increase in the unit cell volume compared to undoped BFO accompanied by a reduction of the rhombohedral distortion (Table S1, Supplementary materials). The chemical bond angle Fe-O-Fe increases wherein the Fe-O bond lengths change to be more equal, thus tending to form more symmetric oxygen octahedra as compared to the undoped BFO (Supplementary materials, Table S1). The refinement of the NPD pattern allowed us to estimate an oxidation state of the cations, which is an oxidation state 3+ for iron ions in accordance with the chemical formula. The oxidation states of the bismuth and lanthanum ions, ~2.8 and 3.5, respectively, are in accordance with the electronegativity values attributed to these ions ~2.05 and 1.1, respectively, which leads to a certain fluctuation in the charge densities along the chemical bonds Bi/La – O. The calculated values of the ion occupation confirm the nearly stoichiometric composition of the material consistent with the chemical formula $Bi_{0.95}La_{0.05}FeO_3$. Thus, the amount of the defects in the material bulk is well below 1%, which is close to an accuracy of the NPD refinement.
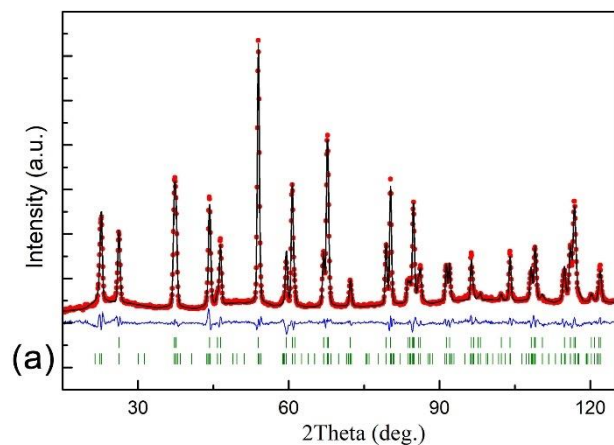
Figure S1. NPD spectra of the BLFO ceramics.

Table S1. Unit cell parameters of $Bi_{0.95}La_{0.05}FeO_3$ calculated using X-ray diffraction and neutron powder diffraction data.

R-phase: R3c space group; Rp = 4.65					
a = 5.5789(5) Å, c = 13.8554(6) Å					
6a (0, 0, z); 18b (x, y, z)					
site	x	y	z	occ	BVS
Bi/La (6a)	0	0	0.0	96.5%	2.822/
				4.9%	3.484
Fe (6a)	0	0	0.2223 (4)	99.9%	
O (18b)	0.4473(3)	0.0176(5)	0.9535 (4)	99.9%	1.996
BFO init. a=3.9425; c=4.0011	c*/a*= 1.0148 rhomb angle 89.43°	La5%BFO a=3.9448; c=3.9997	c/a= 1.0136 rhomb angle 89.47°		
Vol	373,14 /62.19	Vol	373.46 /62.24		
Bi – O			2.531/ 2.284		
Fe – O - Fe	154.99		155.4°		
Fe – O [1,2]	1.943 /2.115		1.947/ 2.109		

2. Time-of-flight secondary ion mass spectrometry (ToF-SIMS) characterization

The sample surface chemical composition was investigated with the use of ToF-SIMS (see details in the main text of the manuscript). ToF-SIMS sputtering depth profiles were used to characterize surface contamination layer and layer with the structural defects: bismuth, iron and oxygen vacancies. ToF-SIMS sputtering profiles revealed a thin surface layer of adsorbates resolved in the depth profiles of Na, K and C-H as a large peak of the intensity near the surface (Figure S2a). Signals of the contamination species decrease significantly with sputtering time (Figure S2a), which proves that they are present only on the surface. The half-width of the peaks responsible for the hydrocarbon contamination of about 1 nm width determines the average thickness of the contamination layer. Comparison of the correlative piezoresponse force microscopy (PFM) image and ToF-SIMS chemical map of the adventitious carbon distribution does not reveal any spatial correlations between spontaneous polarization and distribution of adsorbates (Figure S2b-d).
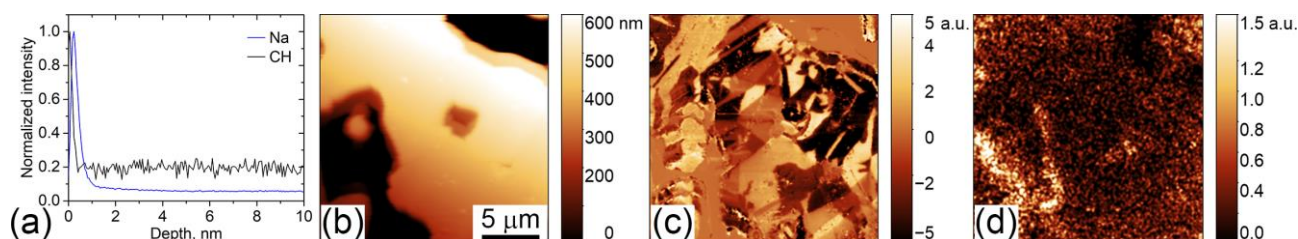

Figure S2. (a) ToF-SIMS sputtering profile of the Na^+ and CH^+ ions, (b) topography, (c) PFM image and (c) ToF-SIMS chemical map of the CH^+ distribution.

3. X-ray photoelectron spectroscopy (XPS) and energy-dispersive X-ray spectroscopy (EDS) analysis

XPS and EDS analysis were used to probe the defect state of the surface. These two methods possess drastically different depth resolution. XPS probes up to a 5 nm-thick surface layer, while EDS captures signal from a depth up to 500-1000 nm from the surface. XPS survey spectrum of BLFO demonstrates only signals from Bi, Fe, La, O, and surface carbon contamination (Figure 5c in the main text of the manuscript). A more detailed analysis of core-level bands reveals fine structure, i.e., components of the Bi 4f doublet: Bi $4f_{7/2}$ at 158.5 eV and Bi $4f_{5/2}$ at 163.8 eV binding energy, components of the La 3d multiplet: La $3d_{5/2}$ 834.1, 837.6 eV and La $3d_{3/2}$ 850.7, 854.4 eV, and bands related to the O 1s: 529.1 and 530 eV of the lattice

oxygen; and bands related to 531.2 and 532.5 eV of the adsorbed oxygen (Figure S3). The estimated element concentrations are summarized in Table S2.

The detailed analysis of the Fe 2p core level (Figure 5b) was performed to discriminate between Fe^{2+} and Fe^{4+} states at the surface, associated with the reduction or oxidation reactions, respectively (see defect model in Sipporting Information, Section 4). A reference spectra of Fe_2O_3 powder (Sigma Aldrich) were captured for comparison with BLFO data. A good agreement between our Fe_2O_3 spectrum and the data of Kozakov et al. [2] was observed (Figure S4a). Further, the features of the Fe 2p core-level spectra from the BLFO were perfectly overlayed with the spectra of the BFO films obtained by Bein et al. [3] with distinguishable features of the Fe^{3+}: a band at ~710 eV and satellites at the ~719 eV and ~724 eV (Figure S4b). Importantly, both our spectrum and the one from ref. [3] were ~ 1.2 eV shifted to lower binding energies in respect to the Fe 2p peak positions in Fe_2O_3 and the position of the bands in the BFO single crystal studied by Kozakov et al. [2]. Bein et al. attributed the shift of the spectra of the undoped BFO to the reduction of Bi and Fe under a water-desorption-stimulated change of the surface potential [3]. Importantly, they observed the Fe^{2+} band at 708 eV after exposure of the ceramic to water vapor [2,4]. At the same time, a further shift of the spectra observed by Bein et al. after oxygen plasma treatment could not be explained similarly. In turn, our BLFO spectra and the spectra from the BFO single crystal obtained by Kozakov et al. in ref. [2] perfectly coincide after correction for the shift, with no sign of the Fe^{2+} band at 708 eV (Figure S4c). We attribute the shift of the XPS spectra to lower binding energy to a net negative surface potential. According to the map in Figure 4a, the value of the positive potential of the screening charge across the sample surface is by a factor of almost two lower than that of the negative surface potential, which leads to a net negative surface charge.

The exposure of the ceramics to ultra-high vacuum in the XPS spectrometer chamber for two days lead to narrowing of the two Fe^{3+} satellite features in spectra at the ~719 eV and ~724 eV, indicating that the original widening of the peaks in BLFO is caused by the surface-mediated chemical reaction (Figure 5d). The similar widening of the ~719 eV and ~724 eV satellites was observed earlier in $BaFeO_3$ exposed to hydration [5] as well as in oxidized yttrium-iron-garnet films [6] and $La_{1-x}Sr_xFeO_3$ with a large Sr-content [7] (Figure S4e). This phenomenon can indicate either a change of the chemical environment or oxidation of iron at the surface to Fe^{4+}. We assume that the formation of Fe^{4+} at the BLFO surface likely occurs during the final steps of sample polishing with colloidal silica. To evaluate the relative concentrations of Fe^{3+} and Fe^{4+} ions, the Fe $2p_{3/2}$ peak was deconvoluted using parameters of the Fe^{3+} multiplet components (Figure S4f) [8,9]. The approach from ref. [10] was used to discriminate between the

Fe^{3+} and Fe^{4+} states: the difference between the experimental curve and the approximation by the Fe^{3+} multiplet (709.2 eV, 710.3 eV, 711.3 eV, 712.7 eV) was extracted as the Fe^{4+} contribution (a wide band at 713 eV and a narrow band at 711 eV). According to that quantitative analysis, at least 5% of iron is in the Fe^{4+} oxidization state before exposure to vacuum, while a 2-days-long storage in vacuum leads to almost complete recovery of the surface iron into the Fe^{3+} state. The Fe^{4+} state formed on the surface during the SSPFM measurements can be an indication of hole segregation (Supporting Information, Section 4, Equation S3), similar to that at domain walls and other interfaces in undoped BFO ceramics [11]. On the other hand, XPS did not reveal clear signs of Fe^{2+} associated with the reduction reaction (Supporting Information, Section 4, Equation S2).

Table S2. Atomic concentrations of the elements calculated from XPS spectra.

Element	Atomic, %	
	initial	2 days vac
Bi	31.3	40.1
O	47.6	39.9
Fe	17.9	15.6
La	3.2	4.4
	Ratio	
Bi/Fe	1.7	2.6
O/Fe	2.7	2.6
La/Fe	0.2	0.3

According to the XPS element analysis (Table S2), the concentration of bismuth is almost 1.7 higher than that of iron, which assumes migration of bismuth towards the surface. This assumption is confirmed by the ToF-SIM depth profiles (Figure 5b in the main text of the manuscript), where the concentration of Bi decreases and the concentration of Fe grows towards the bulk within 6 nm from the surface, which shows a recovery of the stoichiometry. This conclusion can be additionally supported with the data of the EDS analysis, where the probed depth is larger, around 1 μm. The EDS yielded a Bi/Fe ratio of ~1.07, i.e., much closer to the bulk value (Table S3).
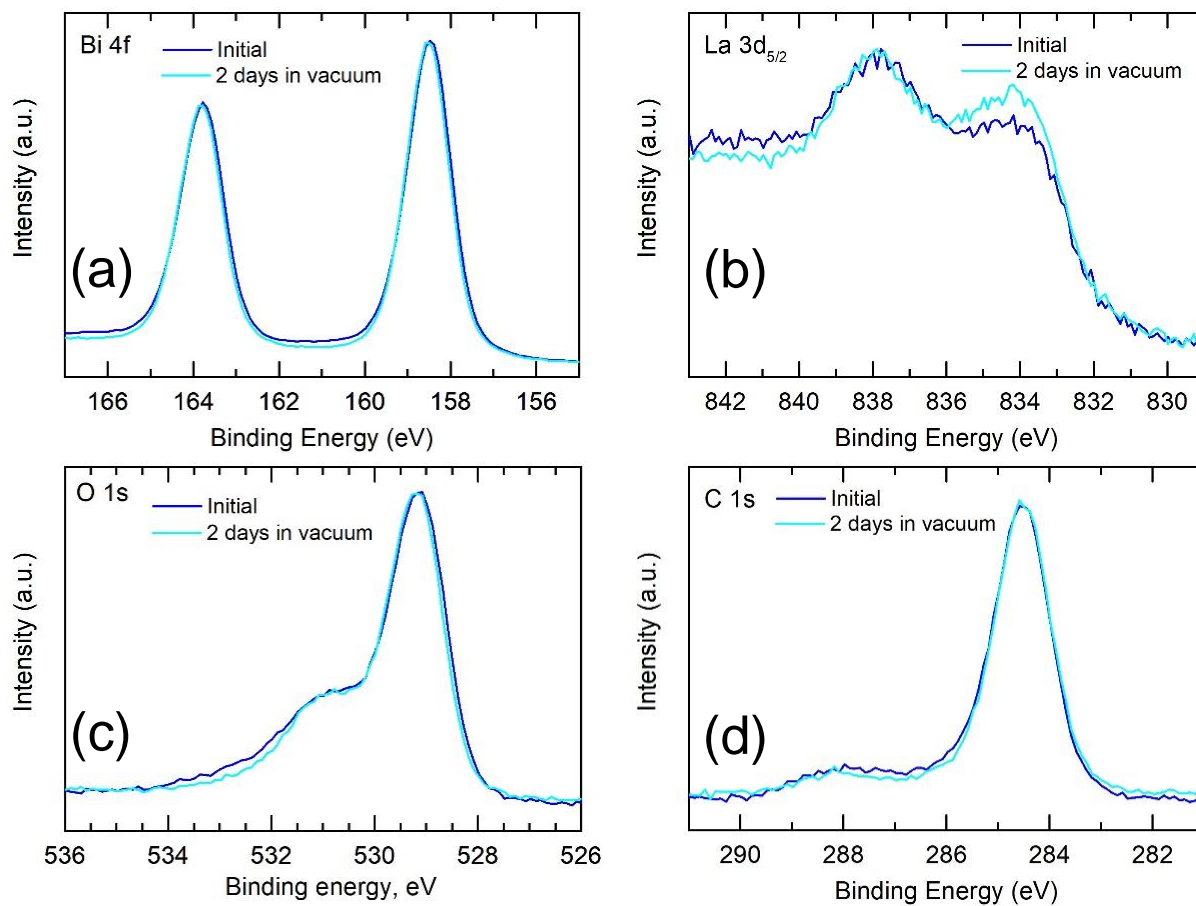
Figure S3. Core-level XPS spectra of Bi, La, O and C in the BLFO ceramics just after place in the vacuum camera of the spectrometer and after 2 days vacuum exposure.
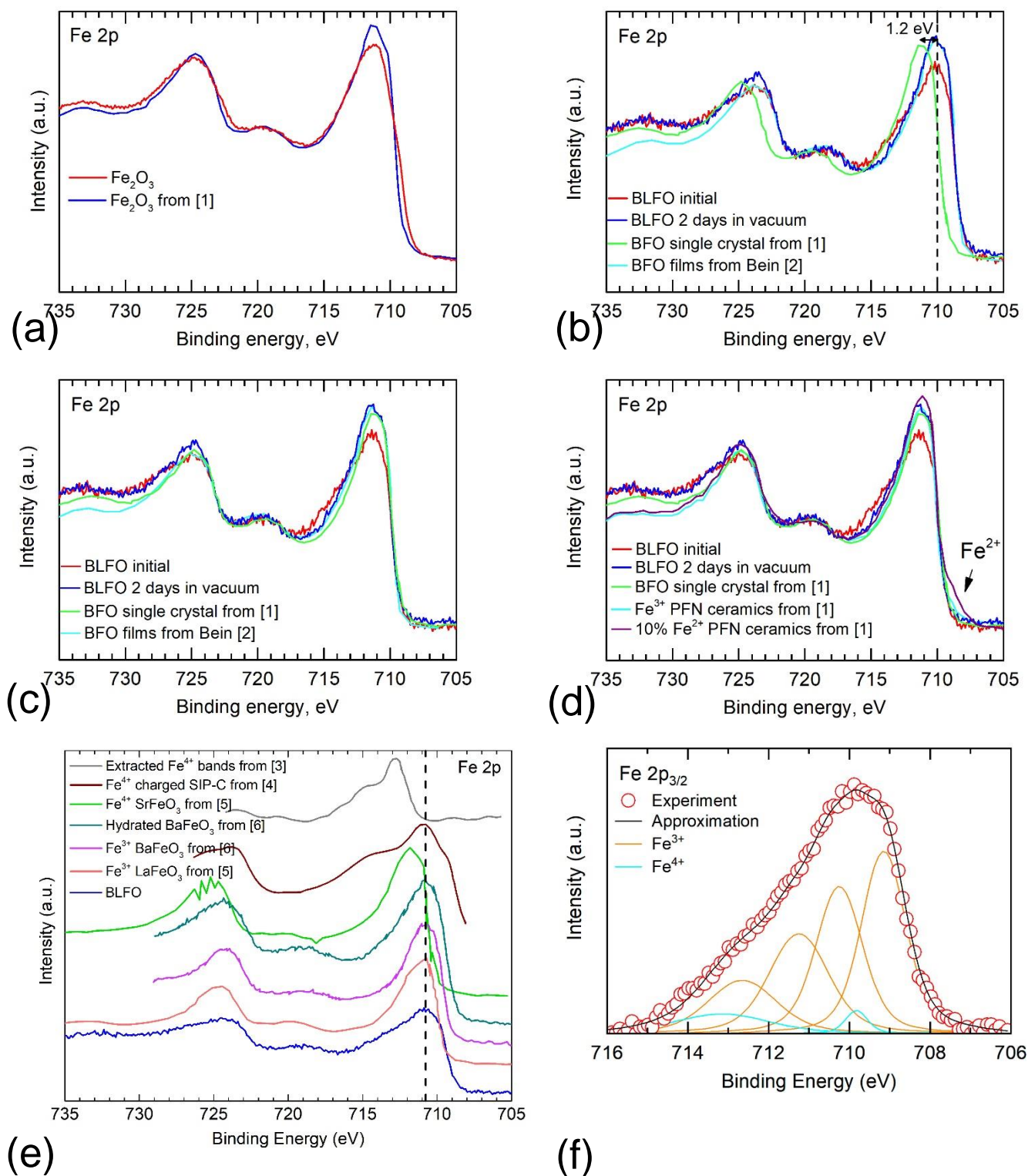
Figure S4. (a) of the measured Fe 2p XPS spectra of Fe_2O_3 powder with the reference literature data from [2]. (b),(c) Comparison of the measured Fe 2p XPS spectra of BLFO ceramics with the reference literature data for the BFO single crystal [2] and BFO thin films [3] (b) before and (c) after shift of the measured spectra and spectra of the BFO thin films from [3] at 1.2 eV to higher binding energies. (d) Comparison of the measured Fe 2p XPS spectra of BLFO ceramics with the reference literature data after 1.2 eV shift to higher binding energies with the spectra of the BFO single crystal [2] and modelled PFN ceramics spectra with pure Fe^{3+} composition and 10% of Fe^{2+} ions. Fe^{2+} band at ~ 708 eV is indicated. Comparison of the measured Fe 2p XPS spectra of BLFO ceramics just after place in the vacuum camera of the

spectrometer with the different literature reference data for the materials containing Fe^{4+} ions at the surface [2,3,6,7,12,13]. (f) Deconvolution of Fe $2p_{3/2}$ band to Fe^{3+} and Fe^{4+}.
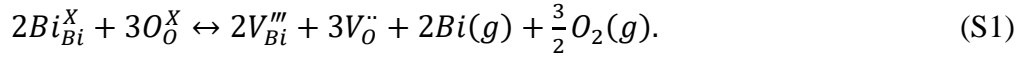
Table S3. Atomic concentrations of the elements calculated from EDS spectra.

| Element	Atomic, %
Bi	13.6
O	52.8
Fe	12.6
La	0.45
C	20.6
	Ratio
Bi/Fe	1.07
O/Fe	4.2
La/Fe	0.04

4. Defect chemistry model

The defect state of the BLFO can be described by the following defect reactions [11,14,15]:

1. Point defect equilibria related to the volatility of Bi_2O_3.

$$2Bi_{Bi}^X + 3O_O^X \leftrightarrow 2V_{Bi}''' + 3V_O^{\cdot\cdot} + 2Bi(g) + \frac{3}{2}O_2(g). \tag{S1}$$

2. Reduction reaction with the formation of the Fe^{2+} oxidization state.

$$2Fe_{Fe}^X + O_O^X \leftrightarrow 2Fe_{Fe}' + V_O^{\cdot\cdot} + \frac{1}{2}O_2(g), \tag{S2}$$
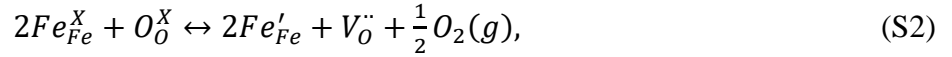
3. Oxidation reaction with the formation of the Fe^{4+} oxidization state.

$$2Fe_{Fe}^X + V_O^{\cdot\cdot} + \frac{1}{2}O_2(g) \leftrightarrow 2Fe_{Fe}^{\cdot} + O_O^X, \tag{S3}$$
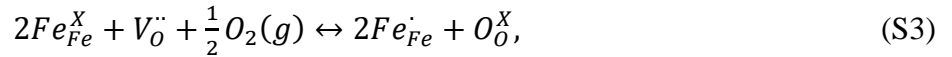
where $2Bi_{Bi}^X, O_O^X, Fe_{Fe}^X$ are normal lattice sites of the Bi, O, and Fe ions, respectively, $Bi(g)$ and $O_2(g)$ are volatile phases. $V_O^{\cdot\cdot},, V_{Bi}'''$ are oxygen and bismuth vacancies, and $Fe_{Fe}^{\cdot}, Fe_{Fe}'$ are iron 4+ and 2+ ions on the iron site, respectively. It is generally accepted that doped bulk ceramic BFO is a p-type conductor [11], while BFO films are n-type conductors [16]. Undoped bulk ceramic BFO was recently shown to be in equilibrium $p = n$ state [15]. The transition to the n-type conductivity associated with the reaction Eq. S2 as well as the formation of Fe^{2+} can happen during annealing of the samples in a reducing atmosphere [17]. Scanning transmission electron microscopy revealed segregation of the $Fe_{Fe}^{\cdot}, V_{Bi}'''$ defects at the domain walls and grain boundaries, while the bulk is defect-free with iron in the Fe_{Fe}^X (Fe^{3+}) state [11]. Schrade et al. [15] suggested a defect model in which the charge of the bismuth vacancies at domain walls should be compensated by oxygen vacancies. Substituting Bi^{3+} ions by La^{3+} should not induce new charged defects and, on the opposite, compensates for the volatility of bismuth ions and stabilizes the crystal structure of the material.

5. Local switching experiments

The internal electric field observed by switching spectroscopy PFM (SSPFM) has a sign opposite to that of the depolarization field (Figure 4 in the main text of the manuscript), and thereby it impedes switching in the forward direction and stimulates backswitching after removal of the bias voltage from the probe. As was discussed in the main text, the switching of upward and downward polarizations should proceed differently because of the difference in the mobility of the positive and negative charged defects participating in the screening of the corresponding bound charges. It was shown that in the case of the switching downward polarization, the stable switching to the upward state is difficult to achieve due to the lack of the mobile screening charge in the material of the negative polarity, which could compensate internal electric field. It leads to the decreasing losses during the polarization reversal and value of the effective piezoelectric coefficient (Figure 4g,h in the main text of the manuscript).

To further trace this difference, local switching experiments were performed in the regions of ceramics with different direction of polarization. NTEGRA Aura scanning probe microscope (NT-MDT, Russia) was used. The external DC voltage pulses to the SPM probe with use of an NI-6251 multifunctional Data Acquisition board (National Instruments, USA) and a high-voltage amplifier Trek-677B (TREK Inc., USA). The grains with preferably out-of-plane oriented spontaneous polarization were selected for measurements, which were distinguished by the maximal values of the out-of-plane piezoresponse and close-to-circular shape of the domains formed after the local switching. A controllable atmosphere with a relative humidity below 5 % was maintained in the microscope chamber using a constant flow of dry nitrogen.

Rectangular voltage pulses of 30 V amplitude and 10 ms-100 s duration were applied successively at a single point in the middle of the domain or at the position of the domain wall (Figure s5a). Then the probe was either immediately withdrawn after the application of the voltage pulses ("withdrawn mode") or left in contact with the surface ("contact mode") [18,19]. Further *ex situ* visualization of the domain structure change was performed using PFM (see method description in the Experimental Section of the main text of the manuscript). The effective radius of the nucleated domains was calculated from the switched areas of newly nucleated domains assuming that the domain shape is approximately circular. In turn, the displacement of the domain wall was determined as the maximal displacement of the domain wall, *d* (as shown in Figure s5a). The dependencies of these two parameters were plotted as functions of the voltage pulse duration (Figure s5b).
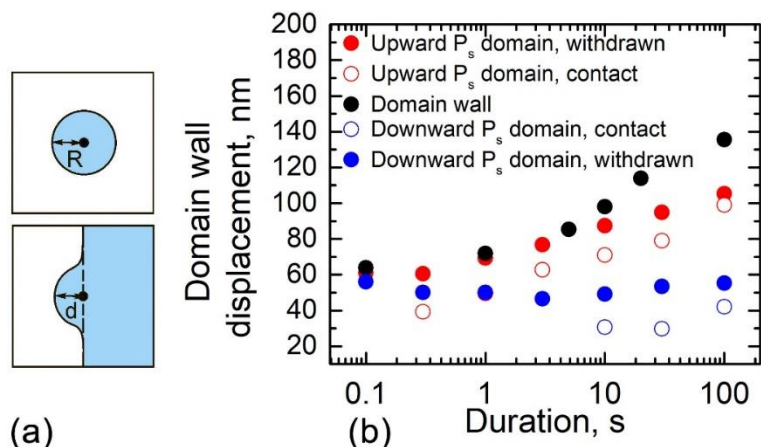
Figure S5. (a) Scheme illustrating how effective domain radius and domain wall displacement has been determined. (b) Dependence of the domain size and domain wall displacement on the duration of the applied voltage pulses extracted from the *ex situ* visualization of the domains after local polarization reversal inside the domain and at the position of the domain wall. The tip was immediately withdrawn after the application of the voltage pulses ("withdrawn mode") or left in contact with the surface ("contact mode").

The domain radius after the local switching in upward domains after the tip withdrawn was close to the value of the domain wall displacement in the case when the voltage was applied on the domain wall, indicating that no significant backswitching happens in this case. It is known that withdrawal of the SPM tip after polarization reversal decreases a backswitching because it decreases the residual depolarization field and limits a charge flow from the SPM tip necessary for the screening of the newly switched domain [20]. In the case of the switching in the upward oriented domain, the final domain radius in the case of the switching in withdrawn and contact mode doesn't vary significantly. However, the radius of the forming domain was smaller than the radius of the domains switched in the "withdrawn mode.", indicating partial backswitching. The backswitched region does not appear in the middle of the reversed domain, which manifests that the backswitching happens under the action of the internal electric field [21] and not due to charge injection under the biased tip [18,22]. The complete backswitching happens only in the case of switching with a duration below 50 ms.

In the downward-oriented polarization case, the switching can be performed in the "contact mode" only if long-time pulses were applied. As well as switching in the "withdrawn" mode results in unstable switching with no apparent dependence of the domain radius on the duration of voltage pulses. The radiuses of the domains were significantly lower than those forming in upward domains. Following the discussion in the main text of the manuscript, the built-in electric field should be compensated by the attracted charged defects of the respective polarity, i.e., bismuth and iron vacancies in the case of the switching in downward oriented polarization, and oxygen vacancies and holes in the case of the switching in upward oriented polarization

(Figure 4b). As bismuth and iron vacancies are low-mobile and cannot move under the external electric stimuli, stable switching cannot be easily achieved in the domain with downward oriented polarization, which induces larger backswithcing of the polarization.

[1]   D. V. Karpinsky, E. A. Eliseev, F. Xue, M. V. Silibin, A. Franz, M. D. Glinchuk, I. O. Troyanchuk, S. A. Gavrilov, V. Gopalan, L.-Q. Chen, A. N. Morozovska, *npj Comput. Mater.* **2017**, *3*, 20.

[2]   A. T. Kozakov, A. G. Kochur, K. A. Googlev, A. V. Nikolsky, I. P. Raevski, V. G. Smotrakov, V. V. Yeremkin, *J. Electron Spectros. Relat. Phenomena* **2011**, *184*, 16.

[3]   N. S. Bein, P. Machado, M. Coll, F. Chen, M. Makarovic, T. Rojac, A. Klein, *J. Phys. Chem. Lett.* **2019**, *10*, 7071.

[4]   C. Lohaus, A. Klein, W. Jaegermann, *Nat. Commun.* **2018**, *9*, 4309.

[5]   J. Landoulsi, M. J. Genet, S. Fleith, Y. Touré, I. Liascukiene, C. Méthivier, P. G. Rouxhet, *Appl. Surf. Sci.* **2016**, *383*, 71.

[6]   Z. Šimša, Šimšová, J. Zemek, P. E. Wigen, M. Pardavi-Horvath, *Le J. Phys. Colloq.* **1988**, *49*, C8.

[7]   L. Wang, Y. Du, P. V. Sushko, M. E. Bowden, K. A. Stoerzinger, S. M. Heald, M. D. Scafetta, T. C. Kaspar, S. A. Chambers, *Phys. Rev. Mater.* **2019**, *3*, 025401.

[8]   A. P. Grosvenor, B. A. Kobe, M. C. Biesinger, N. S. McIntyre, *Surf. Interface Anal.* **2004**, *36*, 1564.

[9]   M. C. Biesinger, B. P. Payne, A. P. Grosvenor, L. W. M. Lau, A. R. Gerson, R. S. C. Smart, *Appl. Surf. Sci.* **2011**, *257*, 2717.

[10] P. C. Rogge, R. U. Chandrasena, A. Cammarata, R. J. Green, P. Shafer, B. M. Lefler, A. Huon, A. Arab, E. Arenholz, H. N. Lee, T.-L. Lee, S. Nemšák, J. M. Rondinelli, A. X. Gray, S. J. May, *Phys. Rev. Mater.* **2018**, *2*, 015002.

[11] T. Rojac, A. Bencan, G. Drazic, N. Sakamoto, H. Ursic, B. Jancar, G. Tavcar, M. Makarovic, J. Walker, B. Malic, D. Damjanovic, *Nat. Mater.* **2017**, *16*, 322.

[12] R. Rajagopalan, B. Chen, Z. Zhang, X.-L. Wu, Y. Du, Y. Huang, B. Li, Y. Zong, J. Wang, G.-H. Nam, M. Sindoro, S. X. Dou, H. K. Liu, H. Zhang, *Adv. Mater.* **2017**, *29*, 1605694.

[13] P. A. Sukkurji, A. Molinari, A. Benes, C. Loho, V. S. K. Chakravadhanula, S. K. Garlapati, R. Kruk, O. Clemens, *J. Phys. D. Appl. Phys.* **2017**, *50*, 115302.

[14] E. T. Wefring, M.-A. Einarsrud, T. Grande, *Phys. Chem. Chem. Phys.* **2015**, *17*, 9420.

[15] M. Schrade, N. Masó, A. Perejón, L. A. Pérez-Maqueda, A. R. West, *J. Mater. Chem.*

C **2017**, *5*, 10077.

[16]   J. Seidel, P. Maksymovych, Y. Batra, A. Katan, S.-Y. Yang, Q. He, A. P. Baddorf, S. V. Kalinin, C.-H. Yang, J.-C. Yang, Y.-H. Chu, E. K. H. Salje, H. Wormeester, M. Salmeron, R. Ramesh, *Phys. Rev. Lett.* **2010**, *105*, 197603.

[17]   M. I. Morozov, M.-A. Einarsrud, T. Grande, *J. Appl. Phys.* **2014**, *115*, 044104.

[18]   M. Lilienblum, E. Soergel, *J. Appl. Phys.* **2011**, *110*, 052018.

[19]   A. V. Ievlev, D. O. Alikin, A. N. Morozovska, O. V. Varenyk, E. A. Eliseev, A. L. Kholkin, V. Y. Shur, S. V. Kalinin, *ACS Nano* **2015**, *9*, 769.

[20]   D. Fu, K. Suzuki, K. Kato, H. Suzuki, *Appl. Phys. Lett.* **2003**, *82*, 2130.

[21]   X. Liu, K. Kitamura, K. Terabe, H. Zeng, Q. Yin, *Appl. Phys. Lett.* **2007**, *91*, 232913.

[22]   A. L. Kholkin, I. K. Bdikin, V. V Shvartsman, N. A. Pertsev, *Nanotechnology* **2007**, *18*, 095502.